A Nanoengineering Approach to Oxide Thermoelectrics For Energy Harvesting Applications

Daniel J. Osborne

Thesis submitted to the faculty of the Virginia Polytechnic Institute and State University in partial fulfillment of the requirements for the degree of

Master of Science
In
Materials Science and Engineering

Jeremiah T. Abiade, Chair
Scott Huxtable
Jean J. Heremans

December 3rd, 2010
Blacksburg, VA

Keywords: oxide thin film, thermoelectric, phonon scattering, metal nanoparticle, thermal conductivity

A Nanoengineering Approach to Oxide Thermoelectrics for Energy Harvesting Applications

Abstract

The ability of uniquely functional thermoelectric materials to convert waste heat directly into electricity is critical considering the global energy economy. Profitable, energy-efficient thermoelectrics possess thermoelectric figures of merit $ZT \geq 1$. We examined the effect of metal nanoparticle – oxide film interfaces on the thermal conductivity κ and Seebeck coefficient α in bilayer and multilayer thin film oxide thermoelectrics in an effort to improve the dimensionless figure of merit ZT. Since a thermoelectric's figure of merit ZT is inversely proportional to κ and directly proportional to α, reducing κ and increasing α are key strategies to optimize ZT.

We aim to reduce κ by phonon scattering due to the inclusion of metal nanoparticles in the bulk of thermoelectric thin films deposited by Pulsed Laser Deposition. XRD, AFM, XPS, and TEM analyses were carried out for structural and compositional characterization. The electrical conductivities of the samples were measured by a four-point probe apparatus. The Seebeck coefficients were measured in-plane, varying the temperature from 100K to 310K. The thermal conductivities were measured at room temperature using Time Domain Thermoreflectance.

Table of Contents

List of Figures

List of Tables

List of Equations

List of Abbreviations
AFM – Atomic Force Microscopy
EDS – Energy Dispersive X-ray Spectroscopy
LAO – $LaAlO_3$
Nb-STO – $SrTi_{0.8}Nb_{0.2}O_3$
PLD – Pulsed Laser Deposition
STO – $SrTiO_3$
TDTR – Time Domain Thermoreflectance
TEM – Transmission Electron Microscopy
XPS – X-ray Photoelectric Scpectroscopy
XRD – X-ray Diffraction

Chapter 1
Introduction

In today's world of ever-decreasing energy sources, it is imperative to use these resources to their maximum potential. We must optimize the efficiency with which we convert raw materials, such as coal, oil, and natural gas, into useful energy. The current efficiencies of internal combustion engines and fossil fuel power plants range from 30 to 38%.[1] This means that 62 to 70 % of the energy available from the raw materials is lost to the surroundings as heat. Much of this waste heat can be recovered directly by thermoelectric power generation devices as electrical current, thus measurably raising the overall energy efficiency of the given process.

Thermoelectric power generators contain no moving parts, produce no waste, and require little to no maintenance. These devices are ideal exemplars of green technology. However, the maximum energy conversion efficiency reported thus far is below 20% for state-of-the-art Bi_2Te_3-based devices.[2] Clearly, this efficiency must be considerably increased if thermoelectrics are to merit a widespread use in automobile engines and power plant exhaust assemblies. A reasonable target efficiency to aim for with thermoelectrics is 30% efficiency. This corresponds to a dimensionless figure of merit ZT = 4, whereas the latest Bi_2Te_3-based devices operate at ZT values slightly above 1.[3] ZT is a number that is a direct measure of the efficiency of a thermoelectric material, and it will be discussed in detail later.

The direct conversion of heat to electrical current by thermoelectric materials is known as the Seebeck effect. In general, when two different electrical conductors, one n-type conducting and the other p-type conducting, are joined in a thermocouple and placed in a temperature gradient, an electrical potential will result, known as the Seebeck voltage. This cross-coupling between heat and electrical currents is illustrated in the diagram below.

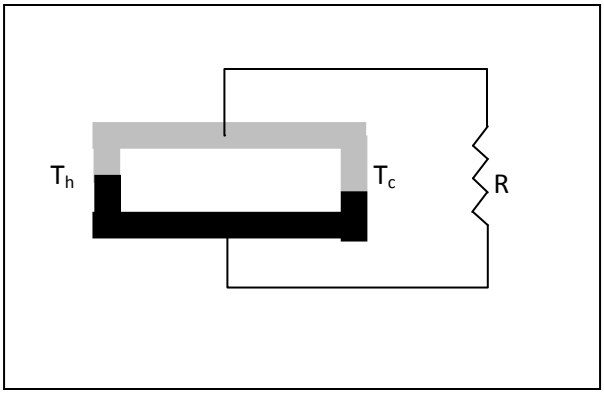

Figure 1 The Seebeck Effect
Two conductors with a heat source at $T = T_h$ and a heat sink at $T = T_c$ at the two junctions, generate a voltage across a resistor R.

The Seebeck voltage generated in a thermocouple is directly related to the temperature difference between the heat source and sink, through a constant of proportionality α. α is called the Seebeck coefficient, and it is a material-specific parameter.

$$\Delta T = T_h - T_c \qquad (1)$$

$$\Delta V = \alpha \Delta T \qquad (2)$$

In order to establish a thermal equilibrium within the thermocouple, hot electrons flow from the hot side of the thermocouple to the cold side, creating an electrical potential: the Seebeck voltage. To maintain this potential, one must maintain the temperature gradient that created the potential in the first place. Thus, one must use materials with low thermal conductivities.

Also, to maximize the potential created by the flow of electrons, the materials used need high electrical conductivities. It follows then, that the energy efficiency of any thermoelectric device depends on both the materials' thermal and electrical conductivities, as well as the materials' respective Seebeck coefficients.

To increase the efficiency of a thermoelectric device, one can take any one of three possible routes: increase the materials' Seebeck coefficients, increase the materials' electrical conductivities, or decrease the materials' thermal conductivities. This thesis will take the third route to improve energy efficiency.

Thermal conduction in solids is mediated by both electrons and phonons. In metals, this process is dominated by electrons, while in semiconductors, phonons are the primary carriers of heat. Since this thesis is solely concerned with the properties of the semiconducting doped oxide, $SrTi_{0.8}\ Nb_{0.2}O_3$, the focus will be on reducing the phonon contribution to the thermal conductivity.

Since phonons are the quanta of lattice vibrations within a crystalline material, the phonon contribution to the material's thermal conductivity is also known as the lattice thermal conductivity. As proposed by Dresselhaus, et.al. and experimentally confirmed by Zide, et.al., the lattice thermal conductivity of a given material may be reduced by introducing nanoparticles within the material. This effect is due to the scattering of phonons by the nanoparticles, and thus will only occur if the nanoparticle size is below the phonon mean free path of the original material.[4],[5]

The goal of this thesis is to reduce the lattice thermal conductivity of $SrTi_{0.8}\ Nb_{0.2}O_3$ by introducing Au or Ni nanoparticles into the oxide matrix. The size of the Au and Ni nanoparticles will vary across the samples made in order to ascertain the optimum nanoparticle size for phonon scattering.

Bi_2Te_3 and PbTe based devices, currently the most efficient of thermoelectrics, can only operate at temperatures below 500 °C, due to their chemical instabilities at higher temperatures.[6] Also, many of the environments in which thermoelectrics may be used to improve the overall energy conversion efficiency of processes are highly corrosive and oxidizing. Both the efficiency and range of applications will be increased if once can increase the reliability and range of temperatures at which a thermoelectric device can operate.

The use of oxide materials that will not undergo serious changes in harsh environments affords one significant improvement in both of these aspects. This thesis will involve the use of the doped oxide $SrTi_{0.8}\ Nb_{0.2}O_3$, which is a reliable and oxidation-resistant thermoelectric material.

Chapter 2
Theory and Literature Review

2.1 Thermoelectric Effects and Device Efficiency

2.1.1 Thermoelectric Driving Forces and Currents

As mentioned above, thermal and electrical currents are coupled in conducting solids by the Seebeck effect. The Seebeck effect is only one example of the more general phenomena of physical driving forces coupling with multiple currents, as described by the thermodynamics of irreversible processes. The following sections will follow the derivations found in the book by Cadoff and Miller.[6] In general, driving forces X_k such as pressure, concentration, temperature, and electric and magnetic potential gradients produce currents such as diffusion, thermal, spin, and electrical currents J_i via equation (3), where the L_{ik} are kinetic transport coefficients:

$$J_i = \sum_k L_{ik} X_k \quad (3)$$

In the specific case of thermoelectric materials, there are two driving forces: a temperature gradient and an electrical potential, both of which drive the thermal and electrical currents. Let us consider for now a system with one-dimensional driving forces and currents. Here, the L_{ik} form a two by two matrix, which is symmetric according to Onsager's reciprocity theorem (4).

$$L_{ik} = L_{ki} \ \ for\ i \neq k \quad (4)$$

In order to make the appropriate choices of forces and currents, we will begin with the following observation: at its thermodynamic equilibrium, a system's total entropy is a maximum with respect to the properties which describe the system, such as temperature and electrical charge. These properties may be denoted by y_i when the system is at equilibrium, and when the system is away from equilibrium, by y_i', thus the deviation of these non-equilibrium values from their equilibrium values is $Y_i = y_i' - y_i$. By definition then, Y_i is zero at equilibrium, and as the entropy S is also a maximum at equilibrium, the difference of the entropy from its equilibrium value may be expressed as in equation (5), where the g_{ik} are the specific Gibbs functions.

$$\Delta S = -\frac{1}{2}\sum_{ik} g_{ik} Y_i Y_k \quad (5)$$

The currents of the system are simply the time derivatives of the respective properties:

$$J_i = \dot{Y}_i \quad (6)$$

The driving forces are calculated in the following manner:

$$X_i = \frac{\partial(\Delta S)}{\partial Y_i} \quad (7)$$

$$X_i = -\sum_k g_{ik} Y_k \quad (8)$$

Multiplying equations (6) and (8), we find:

$$\sum_i J_i X_i = -\sum_{ik} g_{ik} \dot{Y}_i Y_k = \frac{d(\Delta S)}{dt} \quad (9)$$

Therefore, in order to discover the driving forces and currents of a given system, one can write an expression for the change of the system's entropy with time in terms of the system's properties. Recalling the thermoelectric system of figure 1 from section 1.1, there are 3 points at which entropy is produced: the hot and cold ends at the two junctions of the conductors, and the resistive load. We denote the cold end at temperature T_c by "A", the hot end at temperature $T_c + \Delta T$ by "B" , and the resistive load by "C". Thus we have:

$$\Delta S = \Delta S_A + \Delta S_B + \Delta S_C \quad (10)$$

The Gibbs equation tells us, that, for a given change in entropy S at temperature T with a voltage ΔV and charge q, there is an associated energy ΔU:

$$\Delta U = T\Delta S - q\Delta V \quad (11)$$

Thus, for our thermoelectric system, with $T = T_c$ we may rewrite equation (10) as:

$$\Delta S = -\frac{\Delta U}{T} + \frac{\Delta U}{T+\Delta T} - \frac{q\Delta V}{T} \quad (12)$$

.

The resistive load possesses a voltage ΔV by virtue of the Seebeck effect, and we are assuming it is at the same temperature $T = T_c$ as the cold end for simplicity's sake. There is a negative sign in the first term on the right due to the fact that energy is being lost by the cold end, whereas energy is entering the system at the hot end.

Taking the derivative of equation (12) with respect to time, and assuming the temperature difference ΔT and voltage ΔV are maintained across the system, we have:

$$\frac{d(\Delta S)}{dt} = -\frac{dU}{dt}\left(\frac{1}{T}\right) + \frac{dU}{dt}\left(\frac{1}{T+\Delta T}\right) - \frac{dq}{dt}\left(\frac{\Delta V}{T}\right) \quad (13)$$

Multiplying the first two terms on the right hand side by (T+ΔT)/(T+ΔT) and T/T, respectively, and simplifying, we obtain:

$$\frac{d(\Delta S)}{dt} = -\frac{dU}{dt}\left(\frac{\Delta T}{T^2}\right) - \frac{dq}{dt}\left(\frac{\Delta V}{T}\right) \qquad (14)$$

Now, we can easily identify the driving forces and currents in the thermoelectric system as follows:

$$X_1 = -\frac{\Delta T}{T^2} \qquad (15)$$

$$X_2 = -\frac{\Delta V}{T} \qquad (16)$$

$$J_1 = \frac{dU}{dt} \qquad (17)$$

$$J_2 = \frac{dq}{dt} \qquad (18)$$

The ”1” subscript refers to the thermal properties, and the “2” subscript refers to the electrical properties. Now equation (3) may be written as follows:

$$\begin{pmatrix} \frac{dU}{dt} \\ \frac{dq}{dt} \end{pmatrix} = \begin{pmatrix} L_{11} & L_{12} \\ L_{21} & L_{22} \end{pmatrix} \begin{pmatrix} -\frac{\Delta T}{T^2} \\ -\frac{\Delta V}{T} \end{pmatrix} \qquad (19)$$

The two diagonal elements L_{11} and L_{22} of the matrix L will be related to the thermal and electrical conductivities, respectively, and the off-diagonal elements will be related to the cross-coupling of heat and electricity.

2.1.2 Derivation of the Thermoelectric Figure of Merit

The efficiency η of a device that generates an electrical power P via an input of energy Q is defined by equation (20):

$$\eta = \frac{P}{Q} \qquad (20)$$

In order to calculate the efficiency of a given thermoelectric device, we must express P and Q in terms of the relevant properties of the device. The power P is simply related to the Seebeck voltage ΔV generated across the resistive load of resistance R:

$$P = \frac{(\Delta V)^2}{4R} \quad (21)$$

$$P = \frac{(\alpha \Delta T)^2}{4R} \quad (22)$$

The factor of ¼ is to due to the fact that for the best performance, precisely one half of the Seebeck voltage is distributed across the resistive load, and the other half is distributed across the rest of the device, which has the same resistance R as the load. To calculate Q in terms of meaningful quantities, we must perform an energy balance at the hot end of the thermoelectric device. First, there is the heat flow Q_F from the hot to the cold end, which may be expressed in terms of Fourier's Law of Heat Conduction. Second, there is a Joule heat Q_J generated by the finite resistances of the two conductors, half of which flows across the load. Third and finally, there is the heat Q_P generated by the Peltier effect due to the current generated by the Seebeck effect. The Peltier effect, complementary to the Seebeck effect, is simply the conversion of an electric current to a heat flux within a material. These three terms are expressed as follows, wherein A_n and A_p , l_n and l_p, ρ_n and ρ_p, κ_n and κ_p are the cross-sectional areas, lengths, electrical resistivities, and thermal conductivities of the n-type and p-type conductors, respectively:

$$Q_F = \left(\kappa_n \frac{A_n}{l_n} + \kappa_p \frac{A_p}{l_p}\right) \Delta T \quad (23)$$

$$Q_J = \frac{1}{2} I^2 R \quad (24)$$

$$Q_J = \frac{1}{2} I^2 (R_n + R_p) \quad (25)$$

$$Q_J = \frac{1}{2} I^2 \left(\rho_n \frac{l_n}{A_n} + \rho_p \frac{l_p}{A_p}\right) \quad (26)$$

$$Q_P = \alpha I T_h \quad (27)$$

Thus, the total heat input Q at the hot end of the thermoelectric device is:

$$Q = Q_F - Q_J + Q_P \quad (28)$$

$$Q = \left(\kappa_n \frac{A_n}{l_n} + \kappa_p \frac{A_p}{l_p}\right)\Delta T - \frac{1}{2} I^2 \left(\rho_n \frac{l_n}{A_n} + \rho_p \frac{l_p}{A_p}\right) + \alpha I T_h \quad (29)$$

The current I is simply the Seebeck voltage divided by the total resistance 2R of the device, in accordance with Ohm's Law.

$$I = \frac{\alpha \Delta T}{2R} \quad (30)$$

$$I = \frac{\alpha \Delta T}{2\left(\rho_n \frac{l_n}{A_n} + \rho_p \frac{l_p}{A_p}\right)} \quad (31)$$

Now, expressing η in terms of P and Q via equations (22) and (29), and after some algebraic simplification, we arrive at equation (32) for the efficiency of a thermoelectric device with a geometry expressed in equation (33):

$$\eta = \frac{\Delta T}{2T_h - \frac{\Delta T}{2} + 4\frac{((\kappa_n \rho_n)^{1/2} + (\kappa_p \rho_n)^{1/2})^2}{\alpha^2}} \quad (32)$$

$$\frac{A_n l_p}{A_p l_n} = \sqrt{\frac{\rho_n \kappa_p}{\rho_p \kappa_n}} \quad (33)$$

$$Z = \frac{\alpha^2}{\left((\kappa_n \rho_n)^{1/2} + (\kappa_p \rho_n)^{1/2}\right)^2} \quad (34)$$

Using equation (34), which is an expression of properties dependent only on the n-type and p-type conductor materials, we may express the efficiency in (32) as:

$$\eta = \frac{\Delta T}{2T_h - \frac{\Delta T}{2} + \frac{4}{Z}} \quad (35)$$

Now, we can see there are two expressions we can change to maximize the thermoelectric efficiency η: ΔT and Z. As can be inferred from equation (34), the maximum Z

for a device is obtained by increasing the materials' Seebeck coefficient α and their electrical conductivities σ_n and σ_p, and also be decreasing their thermal conductivities κ_n and κ_p.

2.2 Literature Review

As mentioned above, there are three routes for increasing a given material's dimensionless figure of merit ZT: increasing α, decreasing κ, and increasing σ. The first two of these three routes will now be discussed in turn.

There are three central methods to increasing the Seebeck coefficient in thermoelectric materials: energy-dependent electron scattering, quantum confinement of electrons in nanoscale materials, and creating a delta-function-shaped electron density of states with respect to energy.

Energy-dependent electron scattering increases α by blocking low-energy electrons from being conducted through the material. This electron filtering may be accomplished by creating rough interfaces in superlattice materials or by embedding materials with quantum dots. These features will break the translational symmetry of the material, resulting in the non-conservation of transverse momentum. Zide et.al., attempted to realize electron filtering by embedding ErAs nanoparticles in $In_{0.53}Ga_{0.47}As/In_{0.53}Ga_{0.28}Al_{0.19}As$ superlattices, but their results were inconclusive.[7]

Heremans, et.al., synthesized nanogranular PbTe samples and achieved an improvement in α over bulk values. They attributed the increased Seebeck coefficient to a larger carrier scatter parameter in the nanograined samples, which results in energy-dependent scattering of electrons.[8]

Dresselhaus, et.al., have proposed that quantum confinement of electrons in low-dimensional materials will increase α through an increase in the electron density of states. This concept has been confirmed by Ohta, et.al., via the synthesis of $SrTiO_3/SrTi_{0.8}Nb_{0.2}O_3$ superlattice thin films. The confinement of electrons in a two-dimensional electron gas at the interfaces in the superlattices resulted in a fivefold increase in α over bulk values. The 2D electron gas ZT at room temperature was reported as 2.4, but the presence of the insulating $SrTiO_3$ barriers between the 2D electron gas interfaces reduced the effective ZT to 0.24.[4],[9]

Hicks, et.al., have also achieved a high α through quantum confinement. Molecular beam epitaxy was used to produce $PbTe/Pb_{0.4}Eu_{0.6}Te$ quantum well structures. These samples exhibited a high electronic density of states in the PbTe quantum wells, as α and carrier concentration increased with decreasing well thickness. Assuming an electron mobility and a κ similar to bulk values, a room temperature ZT of 2.0 was projected.[10]

A delta-function-shaped electronic density of states centered around the Fermi energy will increase α. Heremans, et.al., have synthesized Tl-PbTe polycrystalline pellets wherein addition of Tl to PbTe has created a sharp peak in the electronic density of states near the Fermi energy. The increase in ZT to 1.5 versus Na-PbTe may be attributed to the enhancement in α due to the effect of adding Tl.[11]

Heat is conducted in materials by both electrons and phonons. Since the electronic contribution κ_e to a material's overall thermal conductivity is directly related to the material's electrical conductivity via the Wiedemann-Franz Law, equation (36), it is typically difficult to reduce the electronic thermal conductivity without also reducing the electrical conductivity.

$$\kappa_e = \sigma L T \qquad (36)$$

$$L = 2.44 \times 10^{-8} watt \times ohm \times K^{-2} \qquad (37)$$ a material-independent constant

Thus, much focus has been placed on reducing the phonon contribution to materials' thermal conductivities. Also, the phonon contribution has been seen to dominate the overall κ in semiconductors, which are more commonly used in thermoelectric devices than metals. So, reducing the phonon contribution will have a large effect on the overall material thermal conductivity.

Phonons are simply the quanta of lattice vibrations, and so the phonon contribution to a material's thermal transport is also called the lattice thermal conductivity: κ_L. Scattering of phonons is the central route to reducing κ_L. Interfaces between dissimilar materials within a thermoelectric device can scatter phonons, and so thermoelectrics composed of layers of different materials stacked on top of each other (known as superlattices) can have reduced κ_L compared to bulk materials.[12]

Costescu, et.al., have achieved this interface phonon scattering by synthesizing W/Al_2O_3 nanolaminates using atomic layer deposition and magnetron sputtering. The small distances between the interfaces between W and alumina layers decrease the overall κ to 0.2 $Wm^{-1}K^{-1}$ at 2.9 nm interface spacing. However, these nanolaminates possess high interface energies which degrade their stability at high temperatures, a quality sought for in thermoelectric power generators which must perform at temperatures approaching 1000 K. [13]

Another example of phonon scattering at material interfaces may be found in the work of Funahashi, et.al. Phonon scattering at the interfaces between layers of Bi_2O_2 and $CoO_{3.5}$ in pressed pellets of polycrystalline $Bi_2Sr_2Co_2O_x$ made by ball-milling reduced κ_L versus bulk values.[14]

Phonon scattering may also be accomplished by using binary compounds known as skutterudites. Skutterudites, such as $CoSb_3$, RhP_3, $IrAs_3$, have large voids which can be filled with heavy ions such as La, Nd, Sm, known as rattlers because they rattle inside the voids. These rattlers' random motion scatters phonons within the material and thus reduce the material's thermal conductivity. [15]

Nanoparticles may be embedded in materials to scatter phonons as well, provided the nanoparticle diameters are less than the phonon mean free path of the host material. Kim, et.al. used molecular beam epitaxy to make samples of $In_{0.53}Ga_{0.47}As$ with ErAs nanoparticles randomly dispersed throughout the $In_{0.53}Ga_{0.47}As$, as well as ErAs/ $In_{0.53}Ga_{0.47}As$ superlattices. The ErAs nanoparticles scattered mid- and long-wavelength phonons, resulting in a reduction in

the thermal conductivity from bulk $In_{0.53}Ga_{0.47}As$ by a factor of 2. The ZT of the ErAs nanoparticle embedded $In_{0.53}Ga_{0.47}As$ was thus increased by a factor of 2 over the bulk values.[5]

Substitution of heavy ions, e.g. Eu^{2+} for lighter ones, e.g. Sr^{2+} has been used to reduce κ_L in $SrTi_{0.8}Nb_{0.2}O_3$ by Kato, et.al. A fifty-percent substitution of Eu^{2+} for Sr^{2+} reduced the phonon mean free path by 12% at room temperature in the Nb-doped STO dense ceramics. This reduction in phonon mean free path translates directly to increased phonon scattering and thus a reduction in κ_L.[16]

Disordered layering of materials may also decrease κ_L, as was shown by Chiritescu, et.al. This group made a layered film structures of WSe_2 via deposition of W and Se sequential bilayers on Si substrates. They found that the thermal conductivity of the layered thin films was 30 times lower than that of single-crystal WSe_2. And though WSe_2 is not a good electrical conductor, disordering stacking may decrease κ_L in other materials besides WSe_2.[17]

Muta, et.al., found that κ can also be decreased by a decrease in crystal symmetry. Ca^{2+} was partially substituted for Sr^{2+} in La-doped STO, and the crystal structure changed from cubic to tetragonal to orthorhombic with increasing Ca^{2+} substitution. The thermal conductivity was decreased from non-substituted La-STO by almost 40% in samples with at least 60% Ca^{2+} substitution.[18]

Increased efficiency is not the only solution for improved thermoelectric devices. Better devices must be able to operate at high temperatures approaching 1000 K, and thus, high temperature stability is important to consider in thermoelectric materials. Oxides offer this stability due to their low potential to oxidize. Both p-type and n-type conducting oxides with promising thermoelectric properties must be found to create an oxide thermoelectric power generation device.

Terasaki, et.al., have found that $NaCo_2O_4$ single-crystals possess a high S ($|S| = 100$ $\mu V/K$), as well as a low electrical resistivity. Thus, despite $NaCo_2O_4$ having a low electron mobility, it is a useful thermoelectric oxide.[19] The stability of $NaCoO_2$ in high humidity has been enhanced by the partial substitution of Sr^{2+} for Na^+, since Na^+ ions are more easily dissolved in water than Sr^{2+}.[20]

Another cobalt oxide that is a good thermoelectric material is $Ca_3Co_4O_9$. La-doping was found to reduce κ via phonon scattering in this oxide. Dynamic forging during processing caused an increase in electrical conductivity due to a high c-axis orientation of the polycrystalline ceramics, the direction of highest electron mobility.[21]

$SrTiO_3$, an insulator that can be doped with La or Nb to become an n-type conductor, has also been found to have good thermoelectric properties. $SrTiO_3$, in either its doped or undoped form, has a perovskite crystal structure, that is, an ABO_3 oxide with a cubic crystallographic symmetry. A and B stand for cations, which are typically metals, and O stands for oxygen. Nb-doped STO thin films were made by Ohta, et.al., and found to have the highest ZT at 1000 K: ZT = 0.37 for 20% Nb-doped films.[22]

Chapter 3
Experimental Methods

3.1 Synthesis

3.1.1 Pulsed Laser Deposition

Pulsed Laser Deposition, or PLD for short, is a unique sputtering technique which may be used to grow thin films, nanoparticles, thin film multilayers, and any combination of these. In short, disc-shaped targets are ablated by an excimer laser and eject a directed plume of atomic-scale particles that deposit themselves on a substrate. This process generally occurs in a vacuum chamber, which may be pressurized with any number of gases if so desired. The substrate may be heated, often in excess of room temperature by several hundred degrees Celsius. The targets are made from powders that may be of any composition and stoichiometry required. Below is a basic illustration of the PLD process.

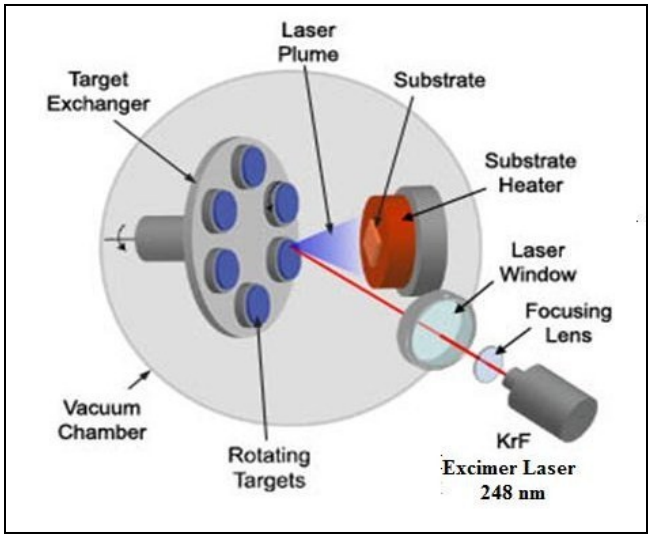

Figure 2 A Pulsed Laser Deposition System

The system used for this thesis involved a KrF excimer laser with an ultraviolet wavelength of 248 nm. Excimer is an abbreviation of the phrase "excited dimer". In our laser, a chamber of Kr and F_2 gas is ionized by an electric discharge of 25 kV and the resulting Kr^+ and F^- ions form excited KrF dimers. Before the ions return to their initial Kr and F_2 gaseous states, they emit light at a 248 nm wavelength.

After exiting the laser, the emitted beam is focused by a UV-transparent glass lens into a 2 mm wide by 3-4 mm tall rectangular spot on the target being ablated. Our typical laser energy is roughly 140-150 mJ, corresponding to an energy density of 1.75 to 2.5 J/cm^2 on the ablated target.

The targets are mounted on a rotating target carrousel that can accommodate as many as six targets at once. During ablation, each target is rastered through a specified angular range and also rotated in order to ensure a uniform ablation across the target's surface. The targets used in this thesis were each commercially made discs of a one inch diameter.

Prior to the deposition of each sample, the vacuum chamber was pumped down to a pressure below 5.0 x 10^{-6} Torr, to ensure a minimal absence of impurities in the samples

deposited. Also, each target was pre-ablated with 1,000 pulses at a 10Hz firing frequency prior to each deposition to create a fresh surface on the target for a quality deposition. During pre-ablation, the substrate was protected from the plume by a shield which was lifted immediately before deposition.

The substrates were heated to a temperature of 650 °C during deposition and immediately afterwards cooled down to 270 °C in the high vacuum at a controlled rate of 5 °C per minute. This was done to grow crystalline samples of a high epitaxial quality. The subsequent cooling to room temperature was uncontrolled. The laser pulse frequency during ablation and deposition was 5Hz.

As mentioned above, samples of varying structure and dimensionality may be grown by PLD. The basics of thin film growth may be applied directly to PLD. Thin film nucleation is controlled by the relationship between the surface energies: γ_s of the substrate, γ_f of the film, and γ_I of the film-substrate interface .

Two-dimensional layer growth, also known as Frank-Van der Merwe growth, occurs if the surface energy of the substrate γ_S is greater than the sum $\gamma_f + \gamma_I$. If the opposite holds: γ_s is less than the sum $\gamma_f + \gamma_I$, the film will nucleate as three-dimensional islands. The growth of islands is called Volmer-Weber growth. Layer growth will transition to island growth if the interface energy γ_I increases with film thickness, and this transition is known as Stranski-Krastanov growth. For metals deposited on oxide surfaces, the transition from layer to island growth occurs in Stranski-Krastanov growth typically occurs after the first atomic monolayer has formed.

Most metals prefer to grow directly as three-dimensional islands on oxide surfaces via the Volmer-Weber growth mode. This is precisely the technique that is used to grow metal nanoparticles on oxide thin film or substrate surfaces with a PLD system.[23],[24]

3.1.2 Deposition of Samples

3.1.2.1 Nb-STO/Au System

In order to control the thickness of the thin films being deposited, and also the approximate diameters of the metallic nanoparticles grown, thickness calibration samples were grown. These samples were each deposited in identical conditions to the subsequent samples to be deposited, though they were cooled at an uncontrolled, higher rate than the controlled 5°C/minute rate used later, since the films' crystallinity was not a concern.

These thickness calibration samples were initially grown on 5x5 mm^2 area $LaAlO_3$ (LAO) substrates, the same substrates to be used for the subsequent samples. For each sample, the substrate was partially masked with another substrate during deposition so that only half of the first substrate was coated, the other half remaining bare. This was done to create a step of film material. The step height was measured by tracing a profilometer tip over the bare portion substrate, the step, and the film itself. This step height was interpreted as the thickness of the

film deposited. The growth rate of the material deposited in the PLD system was then determined by dividing this thickness by the number of laser pulses fired on the target. Thus, one was able to fire a specific number of laser pulses at the target for a specific thickness of material deposited for all subsequent samples.

The first set of thickness calibration samples were grown on small 5x5 mm^2 area LAO substrates, and due to the force of the profilometer tip on these low-area samples, the samples tended to shift at angles with respect to the horizontal during measurements. This shifting resulted in unreliable data, and in some cases, un-readable data concerning the height of the steps. Thus, a second set of thickness calibration samples were grown on much larger silicon wafers of two inch diameters, which gave much more reliable results.

The growth rate of Nb-STO in an oxygen pressure was determined to be approximately 0.367 nm per laser pulse. However, according to a cross-sectional TEM image, Figure 3, of a Nb-STO thin film/Au nanoparticle bilayer sample, the thickness of the Nb-STO film was much lower than expected. The growth rate of Nb-STO was finally determined as 0.046 nm per pulse, using the TEM image as a basis. As a general growth rate for oxides grown by PLD was reported by Strikovski and Miller Jr. as 0.1 nm per pulse, the second estimate of 0.046 nm per pulse was thought to be the more reliable estimate.[25]

The growth rate of Au was determined to be roughly 0.029 nm per pulse in vacuum. The Au thickness calibration sample grown in oxygen tended to delaminate from the silicon substrate upon being lightly brushed with a cotton-tipped swab, and thus was not able to be measured by the profilometer. The growth rate of Au in an oxygen pressure was later confirmed to be the same as in vacuum by the same cross-sectional TEM image mentioned in the previous paragraph.

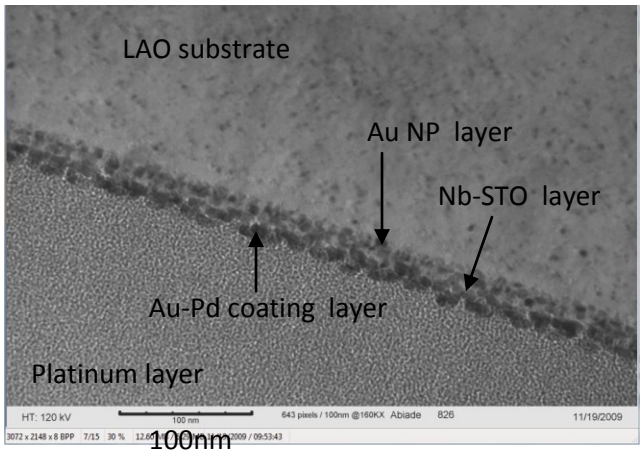

Figure 3 TEM Cross-section Image of D0100309-1X

Initially, in the spring and fall of 2009, all of the samples for this thesis were grown in oxygen with a pressure P_{O_2}= 100 milliTorr. All of these samples, however were insulating films. In other words, these samples all had an infinite resistance, and since the Seebeck effect requires conducting materials, none of these sample were able to generate a Seebeck voltage. They were useful, nonetheless, as this experience and an article by Fukushima and Shibagaki discussing PLD deposition parameters for conductive Nb-STO films led to the conclusion that the oxygen pressure during deposition must be significantly reduced.[26]

A TEM image of the cross-section of the Nb-STO/Au bilayer sample DO100309-1X is shown in Figure 3. The lower left material is platinum from FIB, the next, darker layer is a thin Au-Pd coating deposited post-deposition to make the sample electrically conductive, the next, lighter layer is the Nb-STO thin film, the next layer is the 5nm diameter Au nanoparticle layer, the final layer is the substrate.

Sample DO020210-1X was the first of this thesis' electrically conducting thin films of Nb-STO. The deposition was done in an oxygen pressure between $P_{O_2} = 2.2 \times 10^{-4}$ Torr and 2.5×10^{-4} Torr, which is a range of oxygen pressures about 400 times lower than the samples made previously in 2009. All of the other deposition parameters remained the same as for the samples made in 2009. That is, the film was deposited at a substrate temperature of T = 650°C, and cooled at a controlled rate of 5°C per minute down to 270°C. Also, the frequency of laser pulses fired was 5Hz. Sample DO020210-1X was a very dark shade of navy blue with a resistance R ≈ 300-500 kΩ, as measured with a two-probe handheld voltmeter.

Sample DO020210-1X was deposited on a 5x5 mm^2 LAO substrate. However, since the Seebeck coefficient measurement apparatus requires a sample area of at least 10x10 mm^2 for stable measurement conditions, this sample could not be used. Thus, all subsequent samples (with exceptions that will be noted later) were deposited on 10x10 mm^2 LAO substrates.

In order to have a reference thin film of Nb-STO with no Au nanoparticles present, the next sample, DO021710-1X, was simply a single layer of Nb-STO with a nominal thickness of 540 nm deposited directly onto LAO. All of the deposition parameters were the same as for DO020210-1X except for the size of the substrate. Also, the oxygen pressure P_{O_2} in the chamber during deposition was slightly different than before, but was still within the range of $P_{O_2} = 1.0 \times 10^{-4}$ Torr – 9.9×10^{-4} Torr, as was the case for all the Nb-STO/Au samples. The only reason for the slight differences in oxygen pressure from sample to sample within the Nb-STO/Au sample set was the difficulty in manually maintaining the same very low pressure inside the chamber for as long as an hour by the use of regulator valves alone. Sample DO021710-1X was a translucent blue and had a resistance R ≈ 700 kΩ.

All of the following Nb-STO/Au samples were deposited on 10x10 mm^2 area LAO substrates heated to T = 650°C. They were all deposited in an oxygen pressure in the range $P_{O_2} = 1.0 \times 10^{-4}$ Torr – 9.9×10^{-4} Torr, and cooled in vacuum at 5°C per minute down to 270°C, after which they cooled at an uncontrolled rate to room temperature. The laser pulse frequency was always 5Hz for deposition and 10Hz for pre-ablation.

Sample DO022210-1X was a Nb-STO/Au bilayer sample. The Au nanoparticles of nominally 5nm diameters were deposited directly on top of the LAO substrate, and a nominally 540 nm thick layer of Nb-STO was deposited on top of the Au nanoparticles. DO022210-1X was dark blue with a resistance R ≈ 300 kΩ.

Five Nb-STO/Au multilayers were made during March, 2010. The structure of the multilayers is illustrated in Figure 4. The nominal diameters of the Au nanoparticles in these five multilayers were: 5nm, 10nm, 20nm, 30nm, 40nm. The Nb-STO layers in the multilayers with 5, 10, and 20 nm Au nanoparticles were deposited to have nominal thicknesses of 25nm each, and

the Nb-STO layers in the multilayers with 30 and 40 nm were grown to have nominal thicknesses of 50 nm each. Table 1 lists the seven samples of the Nb-STO/Au system. "NP's" is an abbreviation for "nanoparticles".

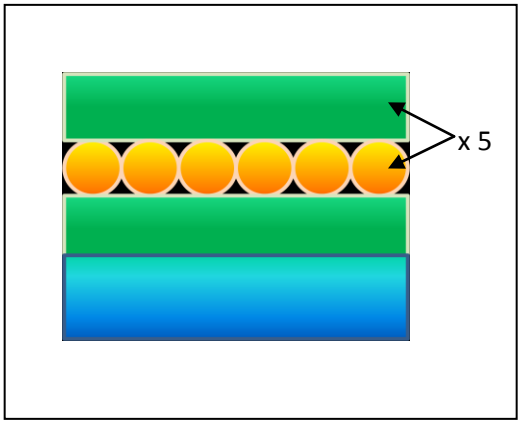

Figure 4 Oxide Thin Film / Metal Nanoparticle Multilayer Structure (Not to Scale) The bottom blue layer represents a LAO substrate, the orange dots represent the metal nanoparticles, of which there are five layers, and the green layers represents the six Nb-STO thin film layers that isolate the individual nanoparticles from each other.

Table 1 Nb-STO/Au Samples

Sample Name	Brief Sample Description	Au Nanoparticle Diameter
DO021710-1X	single layer of Nb-STO	N/A
DO022210-1X	Nb-STO film on top of Au NP's	5 nm
DO030210-1X	Nb-STO/Au multilayer	5 nm
DO031710-1X	Nb-STO/Au multilayer	10 nm
DO031210-1X	Nb-STO /Au multilayer	20 nm
DO031310-1X	Nb-STO/Au multilayer	30 nm
DO031510-1X	Nb-STO/Au multilayer	40 nm

3.1.2.2 Nb-STO/Ni System

As will be described in more detail in Chapter 4, the Nb-STO/Au samples grown in an oxygen pressure in the range P_{O_2} = 1.0 x 10^{-4} Torr – 9.9 x 10^{-4} Torr were very poor conductors of electricity. Taking note of the absence of electrical conduction in the Nb-STO/Au samples that had been deposited in much higher oxygen pressures than this range, it was decided that higher electrical conductivity would occur in samples deposited in the complete absence of oxygen, i.e., in a vacuum. So, all subsequent samples were deposited in vacuum.

Furthermore, as will also be discussed in greater detail in Chapter 4, the inclusion of Au nanoparticles in Nb-STO thin films did not appreciably change the films' thermal conductivity.

So, since such a change had been observed by Shukla, et.al. with Ni nanoparticles in Y_2O_3-stabilized ZrO_2, it was decided to attempt to effect the same change by making Nb-STO/Ni multilayers.[27]

Several attempts at making nickel thickness calibration samples by the same method mentioned above failed to give reliable results. So, in the end, nickel was deposited along with Nb-STO, and the sample was measured via Energy Dispersive X-ray Spectroscopy (EDS), which yields the relative concentration of all the elements in a given sample. From this, the nickel to strontium ratio used along with the known growth rate for Nb-STO to determine the growth rate of nickel: 0.078 nm per laser pulse.

A set of Nb-STO/Ni samples was made in the fall of 2010 with the same basic structures and dimensions as the Nb-STO/Au samples made in March 2010. Each sample was duplicated in order to expedite the characterization process. These samples are listed in Table 2. The L,R (Left, Right) designate a pair of samples made side by side on the substrate heater. These samples were grown on 5x5 mm^2 substrates positioned on the substrate so that they lined up in the middle of the ablation plume, bisecting it. This was done since there was a temporary shortage of 10x10 mm^2 LAO substrates in the lab and these samples could still be used for every other characterization technique except for the Seebeck coefficient measurements.

Table 2 Nb-STO/Ni Samples

Sample Name	Brief Sample Description	Ni Nanoparticle Diameter
DO083110-1X	single Nb-STO layer	N/A
DO090310-1X	single Nb-STO layer	N/A
DO092810-1X	Nb-STO/Ni multilayer	5 nm
DO092910-1X	Nb-STO/Ni multilayer	5 nm
DO100210-1X	Nb-STO/Ni multilayer	10 nm
DO100510-1X	Nb-STO/Ni multilayer	10 nm
DO100610-1X	Nb-STO/Ni multilayer	20 nm
DO100910-1X-L,R	Nb-STO/Ni multilayer	20 nm
DO100910-2X-L,R	Nb-STO/Ni multilayer	30 nm
DO101010-1X-L,R	Nb-STO/Ni multilayer	40 nm
DO101310-1X	Nb-STO/Ni multilayer	30 nm
DO101810-1X	Nb-STO/Ni multilayer	40 nm

3.2 Characterization Techniques

3.2.1 Electrical Conductivity

Since the electrical conductivity σ of a sample of a given material is simply the inverse of its electrical resistivity, which is in turn related to the sample's electrical resistance via the

sample's dimensions, it may seem very straightforward to determine σ for a given material. However, a simple two-point probe resistance measurement using an instrument such as a handheld voltmeter is subject to far too many uncertainties to be a reliable technique. These uncertainties include finite contributions to the measured resistance from the probe-sample contacts and the probe leads themselves.

The extra voltage drops associated with two-point probe measurements, in which the applied current and measured voltage occur at the same two points on the sample, may be eliminated by using a four-point probe technique. In the four-point probe technique used in this thesis, four probes are arranged in a collinear, equally-spaced fashion along the surface of the sample. The two outermost probes provide a passage for an applied current to run through the sample, and the two probes in between these measure the resulting voltage drop across the sample.[28]

Several values of applied current in the milliAmp range were applied across each sample, and the resulting voltage drops in the milliVolt range were read at each value of applied current. Then, for each sample, a plot of measured voltage versus applied current was made. Due to the linear I-V behavior of all the samples, the sample's sheet resistance could be determined using the slope of the linear fit of the data multiplied by a correction factor to account for the finite dimensions of the sample. In the approximation that the probe-spacing of 1.67 mm was larger than the sample thicknesses (which were no more than 0.545 microns), this correction factor was exactly $\pi/\ln(2)$, which is approximately 4.53. This sheet resistance value, when multiplied by the sample thickness, gave the sample's electrical resistivity, which is simply the inverse of the sample's electrical conductivity. Since the substrate material $LaAlO_3$ is a perfect insulator, no correction had to be made for its presence beneath the conducting Nb-STO thin film.

3.2.2 Seebeck Coefficient

The Seebeck coefficient of each of the Nb-STO/Au samples was measured by inducing an in-plane temperature difference of 0.15 to 4 degrees Kelvin across opposite corners of the thin films and measuring the resulting in-plane Seebeck voltage. The cold end temperature of the samples varied from 100 K to 311 K, and the hot end temperature varied from 100 K to 316 K. Thus, the temperature dependence of the samples' Seebeck coefficients were measured from approximately 100 K to 310 K.

A nichrome heating wire was used to create the in-plane temperature difference , which was measured using a solid-state silicon-based thermocouple. The resulting in-plane Seebeck voltage of the sample was measured using copper electrodes with indium-glued contacts on the sample surface. The Seebeck voltage due to the copper electrodes themselves was neglected, since the Seebeck coefficient of copper is very low, only 2 μV/K.

At each temperature, in intervals of 10 degrees K from 100 to 310 K, the Seebeck voltages resulting from temperature differences ranging from about 0.15 K to about 4 K between the hot and cold corners of the sample were measured. For each temperature interval, a linear fit

was made of the Seebeck voltage versus the temperature difference. The Seebeck coefficient was determined as the negative of the slope of the linear fit at each temperature interval. The factor of negative one resulted from the experimental setup of the electrodes.

3.2.3 Thermal Conductivity

The cross-plane thermal conductivities of the Nb-STO/Au and Nb-STO/Ni samples were measured via Time Domain Thermoreflectance (TDTR). TDTR is an optical technique based on the following principle. Since the optical reflectivity of metals has a small temperature dependence, one may generate information concerning heat flow within a material capped with metal by heating the material and measuring its reflectivity. This information about the heat flow in the material is used in conjunction with a one-dimensional heat flow model and the heat capacity of the material in order to determine the thermal conductivity of the material.[27]

Each sample measured was coated with a thin layer of aluminum approximately 100nm thick, to take advantage of the high thermoreflectance of Al at the 800nm wavelength of the laser being used. The Ti:sapphire femtosecond laser is fired at a pulse frequency of 80MHz, and this beam is split into pump and probe beams. The pump beam heats the sample's aluminum-coated surface with a spot size of 27μm and then the probe beam measures the optical reflectivity of the sample with a spot size of 23μm. The optical reflectivity is a direct measure of the temperature decay at the sample's surface, and this information is used in a one-dimensional heat flow model to calculate the thermal conductivity of the sample at room temperature.

The sample is modeled as a series of Nb-STO thin film layers alternating with Nb-STO layers with a Au (or Ni) spherical nanoparticles with a volume fraction of approximately 52.4%, as each nanoparticle is modeled as a sphere touching four adjacent nanoparticle spheres. The bulk thermal conductivities and heat capacities of the component materials: Al, Nb-STO, Au (or Ni), and LAO are used in the model to calculate the multilayer sample's thermal conductivity.

3.2.4 X-ray Diffraction

X-ray diffraction (XRD) is a simple, non-destructive technique that may be employed to measure a sample's crystallographic structure. The most general XRD method is to impinge a narrow, focused beam of X-ray radiation on a sample, and measure the intensity of the diffracted (reflected) beam at various angles with respect to the plane of the sample. Due to the long-range periodicity of the sample's crystalline lattice, the reflected beams will interfere with each other destructively and constructively at regular intervals.

According to the structure and symmetry of the sample being investigated, there will be compound/element-specific peaks in the X-ray intensity as plotted versus twice the angle θ between the detector and the sample surface. Thus, the structure of a sample may be determined by XRD.

Two different XRD machines were used in this thesis: a PAnalytical X'Pert Pro powder XRD machine and a PAnalytical X'Pert PW 3040 MRD single-crystal XRD machine. The powder XRD equipment in Holden Hall is a single-axis machine and is sufficient for the purposes of this thesis. However, since the powder XRD machine was offline at certain times, the multiple-axis PW 3040 MRD single-crystal XRD machine was also used to analyze some samples.

3.2.5 Energy Dispersive X-ray Spectroscopy

Energy Dispersive X-ray Spectroscopy (EDS) uses the characteristic x-rays emitted by materials that have been subjected to an electron beam. These X-rays may be used to determine the relative concentrations of elements within a sample. Using the SEM electron beam at the NCFL, the sampling size of the attached EDS detector is 1x1x1 μm^3. The detection limit on the EDS is roughly 0.1 atomic%.[28]

3.2.6 X-ray Photoelectric Spectroscopy

X-ray Photoelectric Spectroscopy, or XPS for short, is based on the photoelectric effect. This effect is simply the emission of electrons from a material that is being radiated with photons of sufficient energy to excite the electrons out of their respective shells. The monochromatic X-ray source emits photons of energy E_γ at the sample, which in turn emits electrons with kinetic energy E_e. The emitted electrons are collected in a hemispherical energy analyzer, which measures the electron energies via electrostatic means. The difference between the measured electron kinetic energies and the fixed X-ray source energy is the binding energy E_B of the initial bond between the emitted electron and the atom from which it was excited. See equation 38.

$$E_B + E_e = E_\gamma \qquad (38)$$

Since each of the electron shells in each element correspond to a specific binding energy, one can identify the elements within a sample by XPS by determining the various binding energies of the emitted electrons.

XPS is a very surface-sensitive technique. While the incident X-rays may be able to penetrate through the entire bulk of the sample, the emitted electrons are easily scattered as they emerge through the sample. The electrons emitted from deep with the sample quickly lose energy and remained trapped under the surface. Those that are able to emerge after only a few scattering events only contribute to the background of the signal. The peaks in the plot of electron counts versus binding energy are due only to those electrons that do not experience any scattering events while emerging from the sample. These electrons come from roughly the

topmost 10 nm of the sample only. Since the electrons must be allowed a collision-free path from the sample surface to the detector, the sample is analyzed in a vacuum.[29]

3.2.7 Atomic Force Microscopy

Atomic Force Microscopy (AFM) utilizes a micron-sized cantilever beam with a nanometer-sized tip at the very end to yield topographic images of sample surfaces. The cantilever and tip are typically made from silicon or silicon nitride. In contact-mode AFM, the tip is rastered across a region of the sample's surface, and the deflection of the cantilever resulting from the elevation changes along the surface is monitored by a laser reflected from the top of the cantilever into a photodiode.

The resulting topographic data can also be used to determine the average roughness of a sample's surface. Images of areas of 1 square micron and 5x5 μm^2 were taken at 3 different regions on each DO101010-1X-L and DO101010-1X-R, and the corresponding average roughnesses were measured.

3.2.8 Transmission Electron Microscopy

Transmission Electron Microscopy (TEM) involves the imaging of samples by transmitting a high-voltage beam of electrons through the sample onto a detector. Since the deBroglie wavelength of an electron accelerated to a voltage of 100 kiloVolts is approximately $\lambda = 0.004$nm, TEM has a much higher resolution than optical microscopes that use visible light with wavelengths in the range 400 to 700 nm. Using electrons at such high voltages, TEM is able to yield resolution on the order of an angstrom.[28]

Since the sample viewed in TEM must be transparent to electrons, the initial sample must be severely thinned. Focused Ion Beam Lithography (FIB) was used to cut out and thin a cross-section of the Nb-STO/Ni multilayer DO092810-1X for TEM. First, a portion of the sample was coated with platinum for protection during processing, and then sectioned out with a gallium ion beam. This cross-section was thinned and then viewed in the Titan TEM at the Nanoscale Characterization and Fabrication Laboratory (NCFL).

Chapter 4
Results and Conclusions

4.1 Composition and Structure of Samples

4.1.1 XRD Results

The following Figures are XRD patterns of six of Nb-STO/Au samples as measured by the PW 3040 MRD single-crystal XRD machine. As can be seen by the sharpness of the Nb-STO peaks, the films are all highly crystalline. Also, since there are no other Nb-STO peaks besides the (100) and (200) peaks, the films were grown epitaxially on the (100) LAO substrates. However, the complete absence of any Au peaks in these samples indicates that there may not have been enough gold deposited in these samples to show up in the XRD patterns.

The peaks in the XRD patterns were identified using PCPDF data files for $SrTiO_3$ and $LaAlO_3$. According to the literature, the peaks for $SrTi_{0.8}Nb_{0.2}O_3$ are approximately at the same positions as $SrTiO_3$. According to the PCPDF data file for Au, gold has its most intense peaks at 2θ positions and crystallographic orientations: 38.184° (111) and 44.392° (200). No samples had peaks at either of these angles.

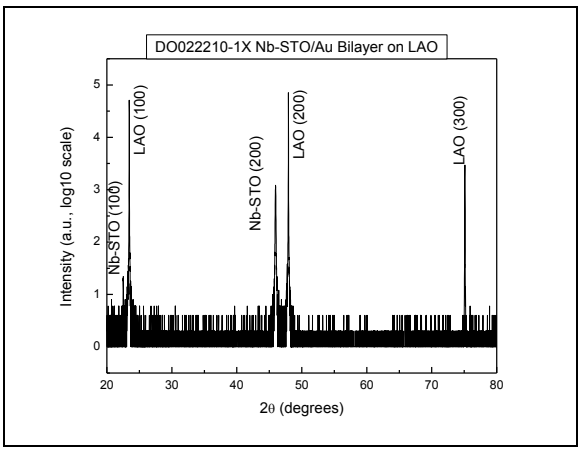

Figure 5 XRD Pattern of DO022210-1X

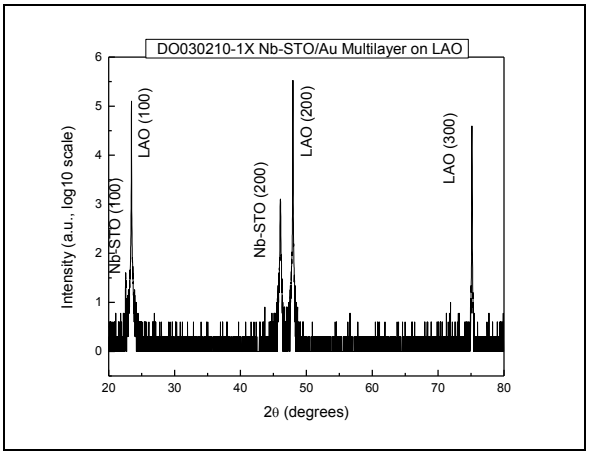

Figure 6 XRD Pattern of DO030210-1X

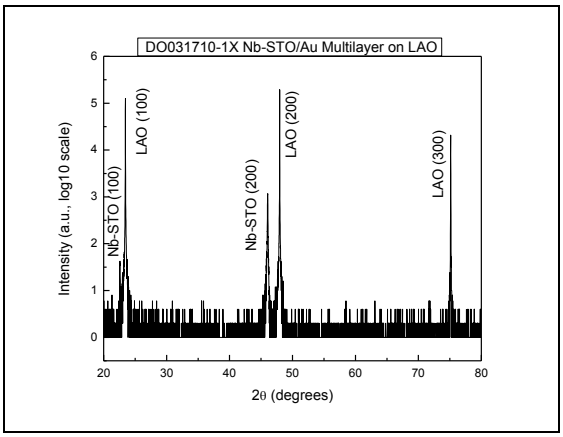

Figure 7 XRD Pattern of DO031710-1X

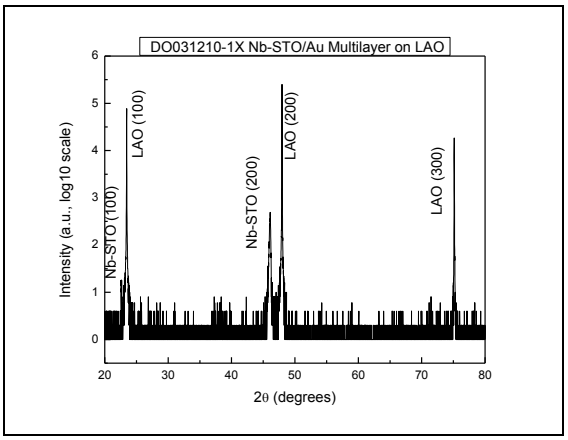

Figure 8 XRD Pattern of DO031210-1X

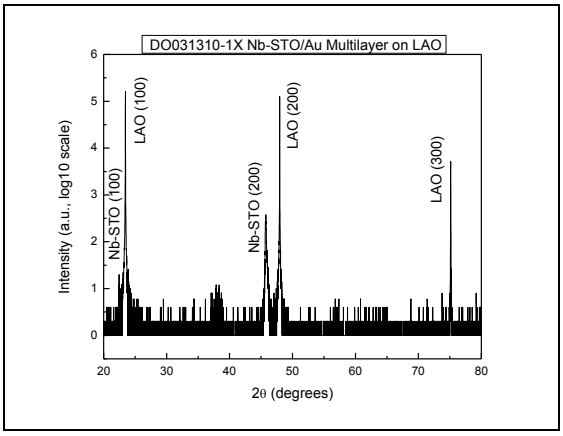

Figure 9 XRD Pattern of DO031310-1X

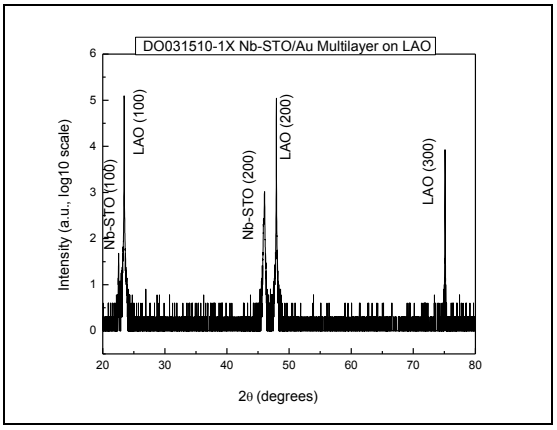

Figure 10 XRD Pattern of DO031510-1X

The XRD pattern for one of the Nb-STO single layer thin film samples grown in the fall of 2010 is shown below.

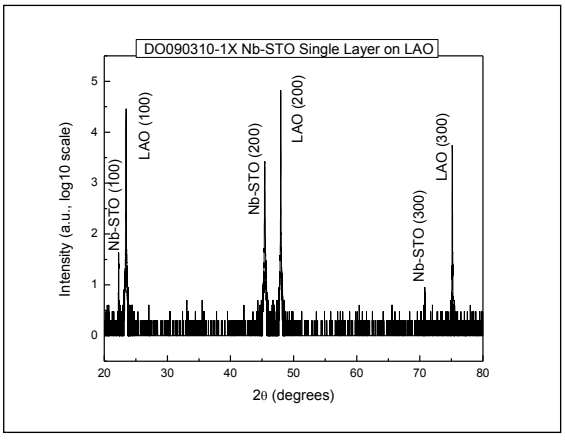

Figure 11 XRD Pattern of DO090310-1X

Shown below is an XRD pattern of DO100510-1X, one of the Nb-STO/Ni multilayers. It is representative of all the Nb-STO/Ni in that the peak pattern is similar among all of these samples. The epitaxial and crystalline quality of the Nb-STO films are similar to those of the Nb-STO/Au samples. However, since both nickel's most intense peak and Nb-STO's most intense peaks are at approximately $2\theta = 45°$, XRD cannot be used to determine the presence of nickel in the Nb-STO/Ni samples.

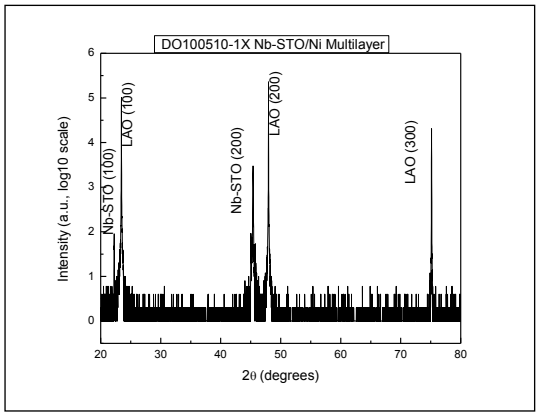

In other words, if the nickel exists in a sample, its peak will be dominated by the Nb-STO peak.

In conclusion, the XRD data has shown that the Nb-STO deposited in all samples is highly crystalline and epitaxial. However, no evidence for Au was seen in any of the Nb-STO/Au samples' XRD patterns. Also, the presence or absence of nickel in the Nb-STO/Ni samples cannot be determined by XRD alone.

Figure 12 XRD Pattern of DO100510-1X

4.1.2 XPS Results

XPS was performed on the Nb-STO thin film single layer sample DO090310-1X, in order to determine the composition of the sample. Below Figure 13, the atomic concentrations normalized to strontium are displayed in Table 3.

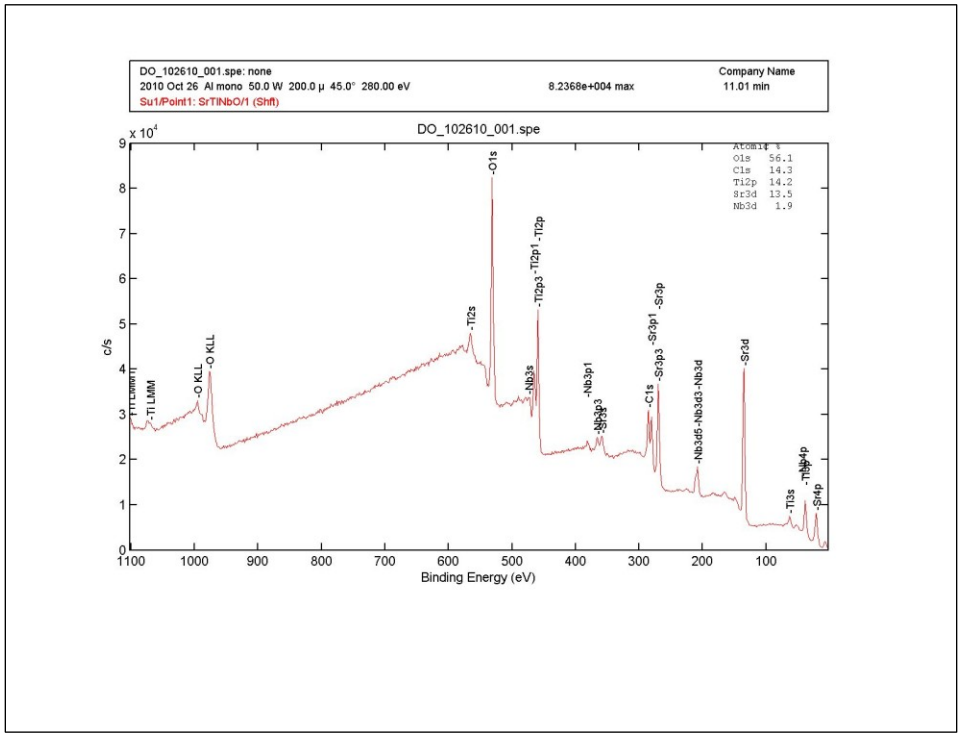

Figure 13 XPS Data for DO090310-1X

Table 3 Atomic Concentrations Normalized to Strontium in DO090310-1X

Element	Concentration Normalized to Sr
Strontium	1
Titanium	1.05
Niobium	0.14
Oxygen	4.16
Carbon	1.06

The existence of carbon in the results is simply to due to carbon impurities on the sample's surface. As mentioned in Chapter 3, XPS indicates only the composition of the topmost 10 nm of the sample, so the composition of the entire sample may be slightly different than that indicated by XPS. According to XPS, the surface of DO090310-1X has a lower Nb dopant level than expected, since the ratio of Ti: Nb is nearly 7.5:1, whereas 20 atomic % Nb-doping should result in a Ti:Nb ratio of 4:1.

4.1.3 AFM Results

In order to determine the degree to which the Ni nanoparticles were capped by the topmost Nb-STO layer in the Nb-STO samples, AFM was performed on samples DO101010-1X-L and DO101010-1X-R. These samples were expected to have 40 nm Ni nanoparticles under the Nb-STO top layer, and thus had the highest potential of all the samples to have a very rough surface. A representative AFM image of DO101010-1X-L with roughness data is displayed below in Figure 14.

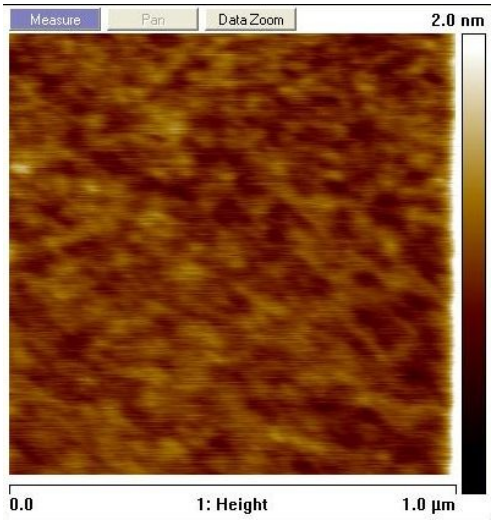

Figure 14 AFM Data for DO101010-1X-L

As indicated by the value of 0.111nm for "Image Ra" in the right-hand column of Figure 14, the average roughness of this one square micron region of DO101010-1X is 1.11Å. AFM data was taken in 3 different regions for each DO101010-1X-L and DO101010-1X-R, and the average roughness in each region was below 5Å. Thus, these samples were very smooth, any Ni nanoparticles were well beneath the samples' surfaces.

4.1.4 TEM Results

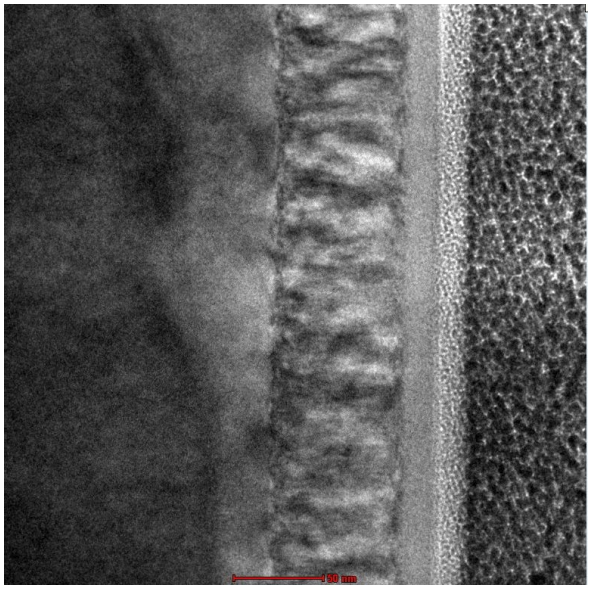

On the left is a TEM image of the cross section of DO092810-1X, a sample that was intended to be a Nb-STO/Ni multilayer with 5nm Ni nanoparticles.

The leftmost layer in Figure 15 is the LAO substrate, and to its right is a Nb-STO thin film approximately 80 nm thick. The Nb-STO film contains no nickel, as confirmed by EDS. Also, the top 10-15 nm of the Nb-STO film, the rightmost portion of it in Figure 15, is amorphous. This is most likely due to amorphatization of the sample during FIB processing. The two rightmost layers in Figure 15 are the platinum coated on the sample to protect it during FIB processing.

Figure 15 TEM Image of cross-section of DO092810-1X with a scale bar of 50 nm

An attempt was made to do TEM on another Nb-STO/Ni multilayer that was expected to have 40 nm Ni nanoparticles. It was hoped that some nickel would be detected in the sample and that nickel nanoparticles would be visible in the cross-section. However, since the ion-mill at the NCFL that would be used to prepare a cross-section of the sample is currently offline, it was not possible to view the sample using TEM.

In conclusion, the Nb-STO thin film / Ni nanoparticle multilayer structure was not observed in the sample DO092810-1X. It is most probable that the nickel growth rate in the PLD system was overestimated, and thus an insufficient amount of nickel was deposited to be detected.

4.2 Transport Properties of Samples

4.2.1 Electrical Conductivity Results

The in-plane electrical conductivity of the Nb-STO/Au samples measured at room temperature is shown in Figure 16, plotted against the nominal diameters of the Au nanoparticles in the multilayers. Except for the multilayer with nanoparticles of 5 nm diameters, the electrical conductivities were on the order of 10^{-3} Ω^{-1} cm^{-1}, which is 6 orders of magnitude below that of the Nb-STO/STO multilayers grown by Ohta, et.al.[9] The room temperature electrical

conductivity of Bi_2Te_3 is also 6 orders of magnitude above the values measured in the Nb-STO/Au samples.[6]

These extremely low values of electrical conductivity led to the conclusion that the samples had a lower doping level than the 20 atomic% Nb that was expected. As mentioned in Chapter 2, the efficiency of a thermoelectric material is directly related to its electrical conductivity. Thus, to obtain the highest efficiency from our materials, we had to increase the electrical conductivity via increased doping.

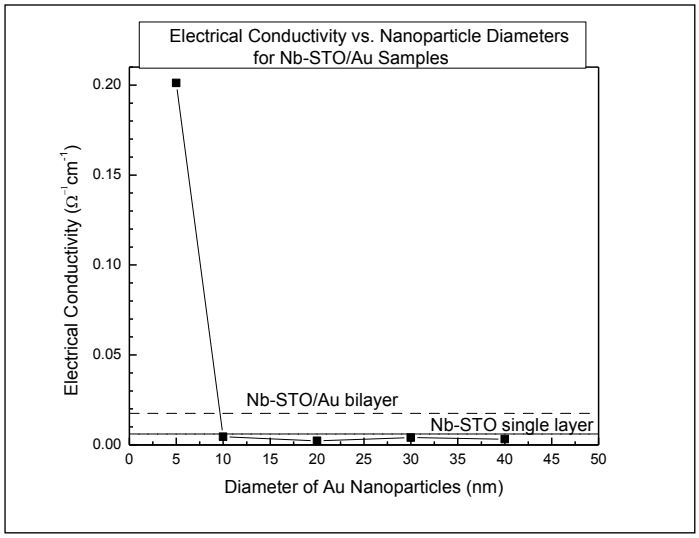

Figure 16 Electrical Conductivities of Nb-STO/Au Samples at Room Temperature

In order to allow for a higher level of Niobium incorporation into the STO crystal structure for higher doping levels, the Nb-STO/Ni samples were grown in vacuum, as noted in Chapter 3. As can be seen in Figure 17, the vacuum deposited samples had electrical conductivities 3 orders of magnitude higher than the Nb-STO/Au samples that had been deposited in oxygen.

There was no significant variation of the electrical conductivity with nominal diameter of the nickel nanoparticles in the Nb-STO/Ni samples. The inclusion of nickel nanoparticles does not seem to effect the electrical conductivity of Nb-STO, as can be readily seen in Figure 17.

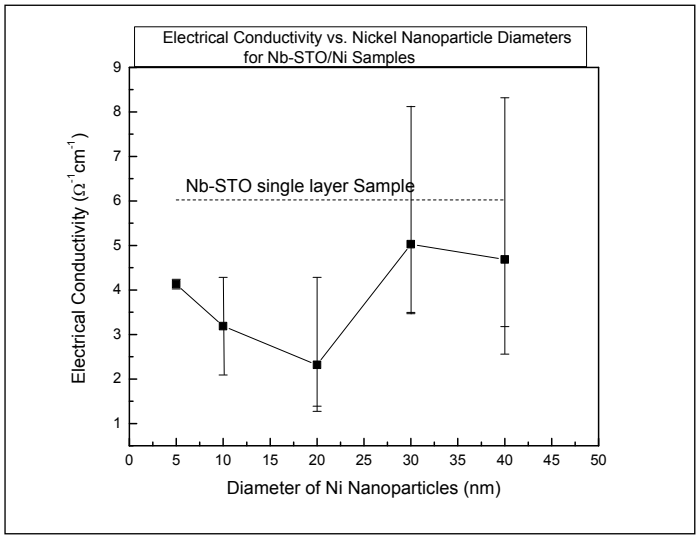

Figure 17 Electrical Conductivity of Nb-STO/Ni Samples at Room Temperature

4.2.2 Seebeck Coefficient Results

The temperature-dependence of the Seebeck coefficients of the seven Nb-STO/Au samples are shown below in Figures 18-24.

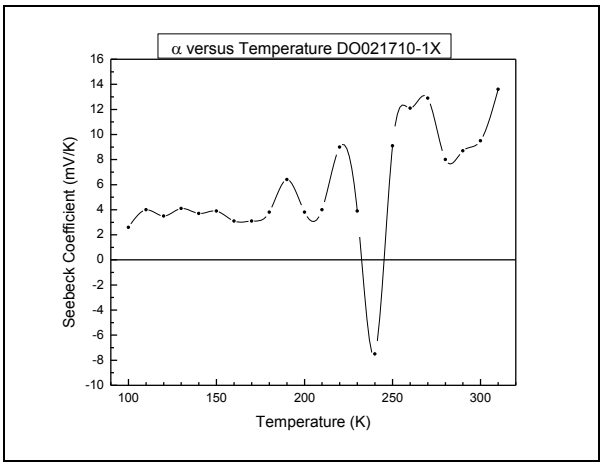

Figure 18 Seebeck Coefficient versus Temperature DO021710-1X

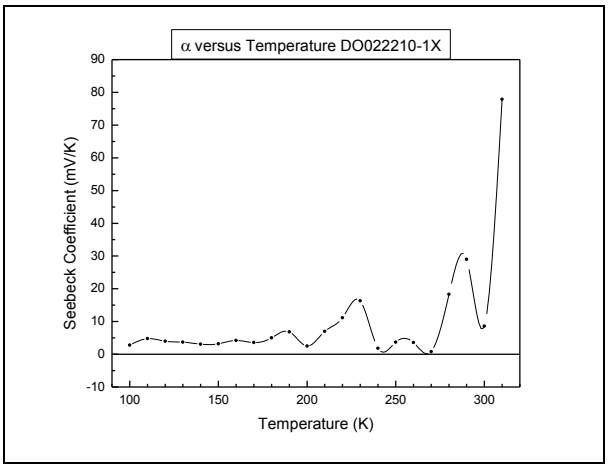

Figure 19 Seebeck Coefficient versus Temperature DO022210-1X

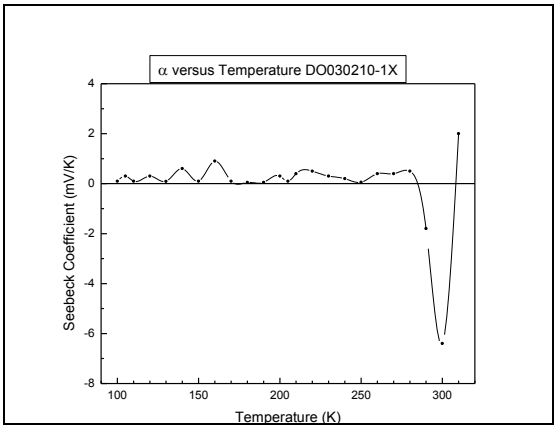

Figure 20 Seebeck Coefficient versus Temperature DO030210-1X

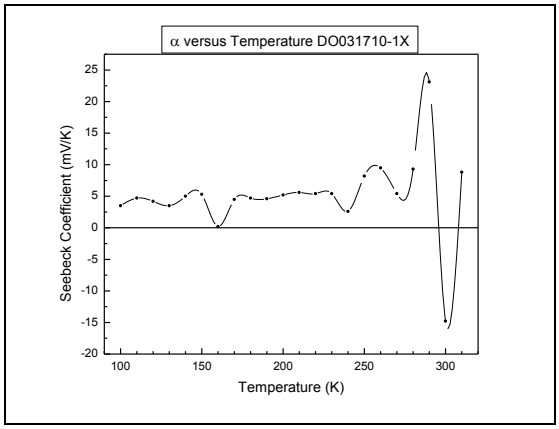

Figure 21 Seebeck Coefficient versus Temperature DO031710-1X

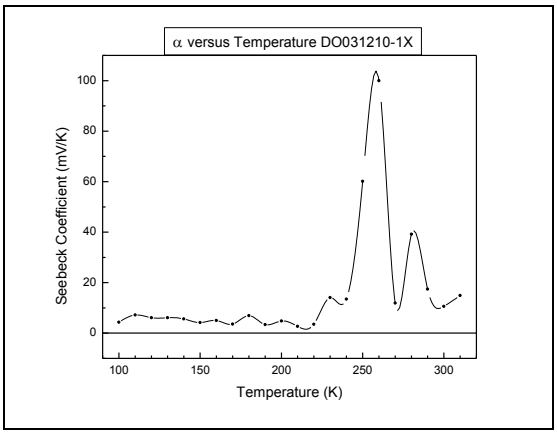

Figure 22 Seebeck Coefficient versus Temperature DO031210-1X

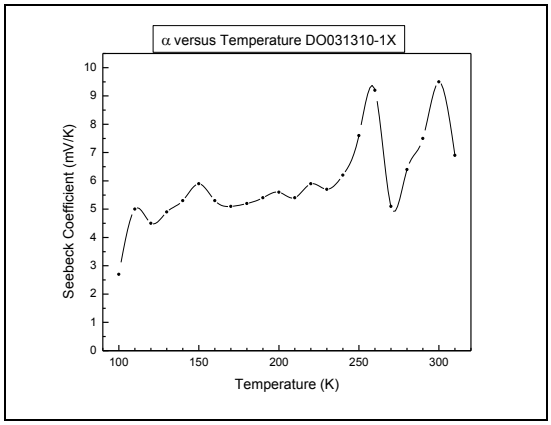

Figure 23 Seebeck Coefficient versus Temperature DO031310-1X

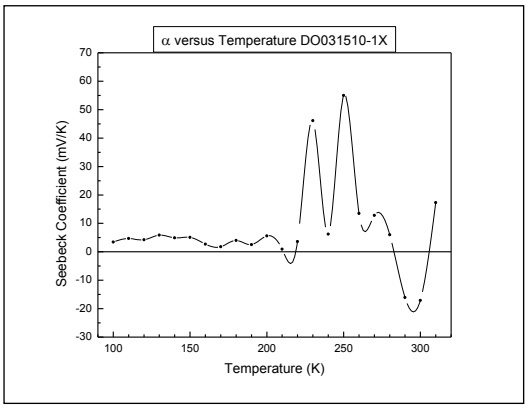

Figure 24 Seebeck Coefficient versus Temperature DO031510-1X

As can be seen in the figures for every sample except for samples DO022210-1X, DO031210-1X, and DO031310-1X, the Seebeck coefficient changes sign as the temperature approaches room temperature. These changes in sign may be attributed to the very low electrically conducting nature of the Nb-STO/Au samples.

Also characteristic of poor electrical conductors is a very large (absolute value) Seebeck coefficient, since the Seebeck coefficient is inversely related to the charge carrier concentration. Large room temperature Seebeck coefficients with absolute values exceeding 5 mV/K are seen in all of the samples. For comparison, the room temperature Seebeck coefficient of Bi_2Te_3, a state-of-the art thermoelectric material with a high electrical conductivity, is approximately 200 μV/K, an order of magnitude lower than observed in our Nb-STO/Au samples.[6]

Neglecting the sign reversals, the Seebeck coefficient of the Nb-STO/Au samples is relatively independent of Au nanoparticle size at room temperature, shown in Figure 25. The Seebeck coefficient is typically modified by doping, and since the Au nanoparticles were not dopants, this behavior is to be expected.

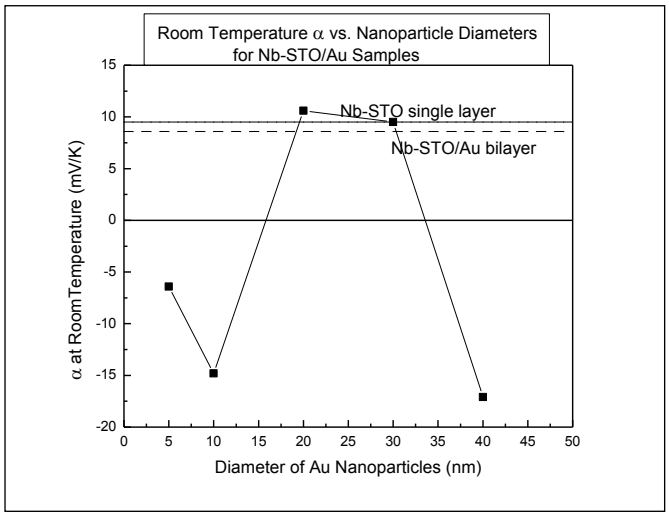

Figure 25 Room Temperature Seebeck Coefficients versus nominal Au nanoparticle size

4.2.3 Thermal Conductivity Results

The thermal conductivity of the Nb-STO/Au samples did not vary significantly with the inclusion of Au nanoparticles in the Nb-STO thin film matrix, as can be seen in Table 4. This is most likely due to the fact that none of the Au nanoparticle diameters are below the 2nm phonon mean free path of bulk STO at room temperature.[30] As mentioned in Chapter 2, phonon scattering by nanoparticles occurs only if the nanoparticles' diameters are smaller than the phonon mean free path of the host material, since the phonon mean free path is the average distance between phonon scattering events.

Table 4 Thermal Conductivities of Nb-STO/Au Samples

Diameter of Au Nanoparticles in Multilayers (nm)	Thermal Conductivity (W/mK)
Nb-STO single layer (545nm thick	3.3
Nb-STO/Au bilayer 5nm Au nanoparticles	3.3
10	3.7
20	3.9
30	3.9
40	3.6

The thermal conductivity did not show a considerable variation with the nominal size of the nickel nanoparticles in the Nb-STO/Ni samples. The second column in Table 5 displays the thermal conductivity data based on the intended Nb-STO/Ni multilayer structures. As was shown in Figure 15, the Nb-STO/Ni multilayer intended to have 5nm Ni nanoparticles had no nickel present, and was thus simply a thin film layer of Nb-STO. The thermal conductivities of the Nb-STO/Ni samples assuming no nickel present in the samples are displayed in the third column of Table 5. These values were calculated assuming a composition of only Nb-STO. A proper interpretation of this data requires knowledge of the microstructure of each sample, which is lacking for the Nb-STO/Ni multilayers samples intended to have 10, 20, 30, and 40nm Ni nanoparticles.

Table 5 Thermal Conductivities of Nb-STO/Ni Samples

Diameter of Ni Nanoparticles in Multilayers (nm)	Thermal Conductivity (W/mK)	Thermal Conductivity (W/mK) assuming no nickel
Nb-STO single layer (500nm thick)	4.3	4.4
5	6.6	3.7
10	5.7	2.7
20	4.45	2.4
30	7.2	6.8
40	4.2	4.3

4.3 Conclusions and Suggestions for Future Work

As the non-renewable energy sources in our world are depleted at ever more rapid rates, the need for improvements in the efficiency with which we convert the raw energy sources into useful electricity increases. Thermoelectric power generators may be used in conjunction with traditional power sources, such as steam-powered coal plants, to convert the waste heat from the plant into useful electricity. However, the efficiency of current thermoelectric generators must be improved to enable a more widespread use of this technique.

The efficiency of a thermoelectric power generator is directly measured by the dimensionless figure of merit ZT. ZT is proportional to the thermoelectric material's Seebeck coefficient α and electrical conductivity σ, and it is inversely proportional to the material's thermal conductivity κ. The goal of this project was to improve the thermoelectric efficiency of $SrTi_{0.8}Nb_{0.2}O_3$ via reducing its thermal conductivity by introducing metallic nanoparticles, either Au or Ni, into the oxide matrix. These metallic nanoparticles were to act as phonon-scattering centers within the Nb-STO thin film matrix, and thus lower the composite's thermal conductivity.

However, the thermal conductivity of the Nb-STO was unaffected by the inclusion of Au or Ni nanoparticles. There are two possible reasons for this lack of change. First, in one of the Nb-STO/Ni samples, there was no nickel detected. Without further investigation of the other Nb-STO/Ni samples, specifically TEM, the existence and structure of nickel within these samples cannot be confirmed or denied. If there is indeed no nickel in any of these samples, then the thermal conductivity should be fairly constant, allowing for slight variations in their deposition.

The second possible conclusion is that since the phonon mean free path of bulk $SrTiO_3$ at room temperature is only 2nm, any nanoparticle larger than 2nm would be ineffective for scattering phonons and reducing the thermal conductivity. If the desired sizes of the Au and Ni nanoparticles were included in the Nb-STO/metal multilayers, the smallest size being 5nm, then a reduction of thermal conductivity is not necessarily a possibility. Shukla, et.al., were able to reduce the thermal conductivity of YSZ by introducing Ni nanoparticles, however, since the phonon mean free path of YSZ is 25 nm, over ten times as large as that of STO.[27],[31]

A suggestion for future work on the Nb-STO/Ni samples already made is TEM characterization of the samples' microstructure to strengthen the conclusions made concerning their thermal conductivity. Also, measurements of these samples' Seebeck coefficients is suggested, in order to determine whether the higher electrical conductivity compared to the Nb-STO/Au samples indeed leads to a lack of sign reversal in the Seebeck coefficient as the temperature varies.

Next, the temperature variation of both sets of samples' electrical and thermal conductivities is suggested to see if there is an improvement in these properties with an increase or decrease in temperature. It would also be good to measure the in-plane thermal conductivity of the samples, or, alternatively, the cross-plane electrical conductivity and Seebeck coefficient. These measurements are suggested because the high in-plane versus cross-plane anisotropy of the samples will have dramatic effects on their transport properties in these different directions. If all three transport properties: α, κ, and σ, could be measured in the same direction, then a ZT specific to the Nb-STO/Au and Nb-STO/Ni samples could be calculated.

Finally, if the 2nm phonon mean free path in $SrTiO_3$ is indeed a limiting factor for thermal conductivity, it is suggested, if possible, to include sub-nm sized metallic nanoparticles in the $SrTi_{0.8}Nb_{0.2}O_3$ matrix to reduce its thermal conductivity. However, since it is difficult to tailor the size of particles below 1 nm using PLD, this may not be easily achieved.

Works Cited

1.) Saqr, Khalid M., Musa, Mohd N., "Critical Review of Thermoelectrics in Modern Power Generation Applications" *Thermal Science* Vol. 13 No.3 165-174 (2009)

2.) Rowe, David M. *Thermoelectrics Handbook: Macro to Nano*. Boca Raton: CRC/Taylor & Francis, 2006.

3.) Fleurial, Jean-Pierre. "Thermoelectric Power Generation Materials: Technology and Application Opportunities" *Journal of Materials* Vol. 61 No.4 (2009)

4.) Dresselhaus, Mildred S.; Chen, Gang; Tang, Ming Y.; Tang, Ronggui; Lee, Hohyun; Wang, Dezhi; Ren, Zhifeng; Fleurial, Jean-Pierre; Gogna, Pawan. "New Directions for Low-Dimensional Thermoelectric Materials" *Advanced Materials* 19, 1043-1053 (2007)

5.) Kim, Woochul; Zide, Joshua; Gossard, Arthur; Klenov Dmitri; Stemmer, Susanne; Shakouri, Ali; Majumdar, Arun. "Thermal Conductivity Reduction and Thermoelectric Figure of Merit Increase by Embedding Nanoparticles in Crystalline Semiconductors" *Physical Review Letters* 96, 045901 (2006)

6.) Cadoff, Irving B, and Edward Miller. *Thermoelectric Materials and Devices: Lectures Presented During the Course on Thermoelectric Materials and Devices Sponsored by the Dept. of Metallurgical Engineering in Cooperation with the Office of Special Services to Business and Industry, New York University, New York, N. Y., June 1959 and 1960*. New York: Reinhold Pub. Corp, 1960.

7.) Zide, J.M.O.; Vashaee, D; Bian, Z.X.; Zeng, G.; Bowers, J.E.; Shakouri, A.; Gossard, A.C. "Demonstration of Electron Filtering to Increase the Seebeck Coefficient in $In_{0.53}Ga_{0.47}As/In_{0.53}Ga_{0.28}Al_{0.19}As$ Superlattices" *Physical Review B* 74 205335 (2006)

8.) Heremans, Joseph P.; Thrush, Christopher M.; Morelli, DonaldT. "Thermopower Enhancement in Lead Telluride Nanostructures" *Physical Review B* 70 115334 (2004)

9.) Ohta, Hiromichi "Thermoelectrics based on Strontium Titanate" *Materials Today*, Vol.10 No.10, (2007)

10.) Hicks, L.D.; Harman, T.C.; Sun, X.; Dresselhaus, M.S. "Experimental Study on the Effect of Quantum-Well Structures on the Thermoelectric Figure of Merit" *Physical Review B* Vol.53 No.16 (1996)

11.) Heremans, Joseph P.; Jovovic, Vladimir; Toberer, Eric S.; Saramat, Ali; Kurosaki, Ken; Charoenphakdee, Anek; Yamanaka, Shinsuke; Snyder, G. Jeffrey. "Enhancement of Thermoelctric Efficiency in PbTe by Distortion in the Electronic Density of States" *Science* 321, 554 (2008)

12.) Böttner, Harald; Chen, Gang; Venkatasubramanian, Rama. "Aspects of Thin Film Superlattice Thermoelectrics Materials, Devices, and Applications" *MRS Bulletin,* Vol.31, (2006)

13.) Costescu, R.M.; Cahill, D.G.; Fabreguette, F.H.; Sechrist, Z.A.; George, S.M.. "Ultra-Low Thermal Conductivity in W/Al_2O_3 Nanolaminates" *Science* 303 989 (2004)

14.) Funahashi, Ryoji; Matsubara, Ichiro; Sodeoka, Satoshi. "Thermoelectric Properties of $Bi_2Sr_2Co_2O_x$ Polycrystalline Materials" *Applied Physics Letters* Vol.76 No.17 (2000)

15.) Nolas, G.S.; Morelli, D.T.; Tritt, Terry M. "Skutterudites: A Phonon Glass-Electron Crystal Approach to Advanced Thermoelectric Energy Conversion" *Ann. Rev. Materials Science* 29:89-116 (1999)

16.) Kato, Keisuke; Yamamoto, Masahiro; Ohta, Shingo; Muta, Hiroaki; Kurosaki, Ken; Yamanaka, Shinsuke; Iwasaki, Hideo; Ohta, Hiromichi; Koumoto, Kunihito; "The Effect of Eu Substitution on Thermoelectric Properties of $SrTi_{0.8}Nb_{0.2}O_3$" *Journal of Applied Physics* 102 116107 (2007)

17.) Chiritescu, Catalin; Cahill, David G.; Nguyen, Ngoc; Johnson, David; Bodapati, Arun; Keblinski, Pawel; Zschack, Paul. "Ultralow Thermal Conductivity in Disordered, Layered WSe_2 Crystals" *Science* 315, 351 (2007)

18.) Muta, Hiroaki; Ieda, Akihiro; Kurosaki, Ken; Yamanaka, Shinsuke. "Substitution Effect on the Thermoelectric Properties of Alkaline Earth Titanate" *Materials Letters* 58 3868-3871 (2004)

19.) Terasaki, I.; Sasago, Y.; Uchinokura, K. "Large Thermoelectric Power in $NaCo_2O_4$ Single Crystals" *Physical Review B Condensed Matter (Rapid Communications) Third Series,* Vol.56, No.20 (1997)

20.) Sugiura, Kenji; Ohta, Hiromichi; Nomura, Kenji; Hirano, Masahiro; Hosono, Hideo; Koumoto, Kunihito. "Fabrication and Thermoelectric Properties of Layered Cobaltite, γ-$Sr_{0.32}Na_{0.21}CoO_2$ epitaxial films" *Applied Physics Letters* 88, 082109 (2006)

21.) Lin, Yuan Hua; Lan, Jinle; Shen, Zhijian; Liu, Yuheng; Nan, Ce-Wen; Li, Jing-Feng. "High-Temperature Electrical Transport Behaviors In Textured Ca3Co4O9-based Polycrystalline Ceramics" *Applied Physics Letters* 94 072107 (2009)

22.) Ohta, Shingo; Nomura, Takashi; Ohta, Hiromichi; Hirano, Masahiro; Hosono, Hideo; Koumoto, Kunihito. "Large Thermoelectric Performance of Heavily Nb-doped $SrTiO_3$ Epitaxial Films at High Temperatures" *Applied Physics Letters*, Vol.87 Issue 9, (2005)

23.) Kaiser, Norbert. "Review of the Fundamentals of Thin-Film Growth" *Applied Optics* Vol.41 No.16 3053-3060 (2002)

24.) Campbell, Charles T. "Ultrathin Metal Films and Particles on Oxide Surfaces: Structural, Electronic, and Chemisoprtive Properties *Surface Science Reports* 27 1-111 (1997)

25.) Strikovski, Mikhail and Miller Jr., John H., "Pulsed Laser Deposition of Oxides: Why the Optimum Rate is About 1Å Per Pulse" *Applied Physics Letters* Vol.73 No.12 1733-1736 (1998)

26.) Fukushima, K. and Shibagaki, S., "Niobium Doping Effect on Resistivity of Epitaxially Grown Nb-$SrTiO_3$ Thin Films by Laser Ablation Method" *Journal of Electroceramics* 4:S1 81-90 (1999)

27.) Shukla, Nittin C.; Liao, Hao-Hsiang; Abiade, Jeremiah T.; Murayama Mitsuhiro, Kumar, Dhananjay; Kumar; Huxtable, Scott T. "Thermal Transport in Composites of Self-Assembled Nickel Nanoparticles Embedded in Yttria-Stabilized Zirconia" *Applied Physics Letters* 94 151913 (2009)

28.) Schroder, Dieter K. *Semiconductor Material and Device Characterization*. Piscataway, NJ: IEEE Press, 2006.

29.) Vickerman, John C. *Surface Analysis*. Chichester, UK: Wiley & Sons 1997

30.) Koumoto, Kunihito; Wang, Yifeng; Zhang, Ruizhi; Kosuga, Atsuko; Funahashi, Ryoji. "Oxide Thermoelectric Materials: A Nanostructuring Approach" *Annual Review of Materials Research* 40:363-394 (2010)

31.) Eastman, J.A.; Soyez, G.; Bai, G.-R., Thompson, L.J. "Nanostructured Materials for Microstructural Control of Thermal Properties" *Proceedings of NATO Advanced Study Institute on Functional Gradient Materials and Surface Layers Prepared by Fine Particle Technology,* (2000)